Commensurate helicoidal order in the triangular layered magnet Na$_2$MnTeO$_6$

A. I. Kurbakov [1] A. E. Susloparova,[1] V. Y. Pomjakushin,[2] Y. Skourski,[3] E. L. Vavilova,[4] T. M. Vasilchikova [5]

G. V. Raganyan,[5,6] and A. N. Vasiliev [5,6]

[1] *NRC Kurchatov Institute - PNPI, Gatchina 188300, Russia*
[2] *Laboratory for Neutron Scattering and Imaging LNS, Paul Scherrer Institute, Villigen CH-5232, Switzerland*
[3] *Hochfeld-Magnetlabor Dresden (HLD-EMFL), Helmholtz-Zentrum Dresden-Rossendorf, Dresden 01328, Germany*
[4] *Zavoisky Physical-Technical Institute, FRC Kazan Scientific Center, RAS, Kazan 420029, Russia*
[5] *Faculty of Physics, Lomonosov Moscow State University, Moscow 119991, Russia*
[6] *National University of Science and Technology "MISiS," Moscow 119049, Russia*

The trigonal layered quaternary tellurate Na$_2$MnTeO$_6$ has been studied by means of various techniques to clarify its magnetic properties. The crystal structure of this compound is based on the triangular arrangement of all cations in the parallel layers with the space group $P\bar{3}1c$. By using symmetry analysis of the magnetic neutron scattering data, we have found that the solution for the magnetic structure corresponds to the magnetic Shubnikov group $R\bar{3}'c'$ (No. 167.4.1337). Mn^{4+} ions in an octahedral environment form a triangular network where all spins are directed from the center of each triangle. Overall magnetic structure in Na$_2$MnTeO$_6$ is commensurate 120° spin helix with propagation vector $\boldsymbol{k} = (1/3, 1/3, 1/3)$ in variance with planar spin structure in structurally equivalent Li$_2$MnTeO$_6$ with magnetic propagation vector $\mathbf{k} = (1/3, 1/3, 0)$. The magnetization measurements show that Na$_2$MnTeO$_6$ experiences an antiferromagnetic order at $T_N = 5.5$ K. NMR, electron spin resonance, and thermodynamics experiments demonstrate the extended temperature region of 2D short-range correlations well above the ordering temperature.

I. INTRODUCTION

Low-dimensional magnetic systems are quite sensitive to tiny variations of exchange interaction parameters responsible for the formation of either liquid or long-range ordered ground states. They are similarly susceptible to the effects of single-ion anisotropy following qualitatively different protocols in Heisenberg-type and Ising-type cases. The decisive factor influencing the behavior of low-dimensional magnets is the value of spin moment. The quantum effects are most pronounced at small spin values while the systems based on the ions with large spin values tend to classical magnetism [1]. Triangular magnetic systems are subject to magnetic frustration stemming from the competition of mutually exclusive couplings [2]. In spin $S = 1/2$ or 1 magnets, this frustration often leads to liquidlike behavior at low temperatures [3–5]. Large spin $S = 3/2$ or 5/2 systems lift the frustration by the formation of the long-range ordered magnetic structures. In particular, Heisenberg-type layered systems may reach 120° noncollinear orders of various types [6–8].

The family of trigonal layered quaternary tellurates [9] A_2MnTeO$_6$ ($A =$ Li, Na, Ag, Tl) provides a unique possibility to tune the interlayer exchange interaction parameters leaving virtually intact the parameters of magnetic exchange in the layers [10]. Most important in this respect is the fact that the change in the interlayer spacing influences the ratio of nearest-neighbor and next-nearest neighbor interlayer exchanges. The ions of tetravalent manganese with spin $S = 3/2$

in A_2MnTeO$_6$ form a diluted triangular net within the layer being separated by the hexavalent tellurium ions. The overall arrangement of both Mn^{4+} and Te^{6+} centered edge-sharing octahedra is of the honeycomb type. The interlayer space in these compounds is filled by the dense package of the alkali ions centered face-sharing trigonal prisms. It has been established by neutron powder diffraction that the magnetic structure of the first member in this series, Li$_2$MnTeO$_6$, can be represented by a 120° noncollinear spin arrangement with the propagation vector $\boldsymbol{k} = (1/3, 1/3, 0)$ [11].

Here, we present a study of thermodynamic and resonant properties of another member of the quaternary tellurates family, Na$_2$MnTeO$_6$. The substitution of Na$^+$ for Li$^+$ in A_2MnTeO$_6$ compounds results in a slight increase of 2% in a parameter and a sizable increase of 11% in c parameter of the unit cell. This chemical substitution influences both angles and distances of magnetic exchange pathways. Na$_2$MnTeO$_6$ has been investigated in the wide ranges of temperature and magnetic field in measurements of temperature and field dependences of magnetization M and specific heat C_p, by means of the pulsed magnetic field, electron spin resonance (ESR), NMR, and neutron powder diffraction (NPD).

II. EXPERIMENT

Powder sample of Na$_2$MnTeO$_6$ has been prepared by solid-state synthesis from NaMnO$_2$, NaNO$_3$ and TeO$_2$ at 650–720 °C as described in Ref. [10]. Earlier studied

Li$_2$MnTeO$_6$ sample, whose properties will be compared with the characteristics of its Na-based counterpart, has been prepared by the exchange reactions of Na$_2$MnTeO$_6$ and molten lithium nitrate. The analytical and x-ray diffraction data confirmed the full replacement of sodium by lithium ions in Li$_2$MnTeO$_6$ [10,11].

The magnetization measurements were performed using a Quantum Design superconducting quantum interference device magnetometer MPMS-7T. The temperature dependences of the magnetic susceptibility were measured in a wide range of external magnetic fields: $1 T \leqslant B \leqslant 7 T$ with an increment of 1 in the temperature range 2–50 K. Pulsed-field magnetization was measured at Dresden High Magnetic Field Laboratory [12]. The magnet was energized by a single 1.44-MJ capacitor module. The total pulse duration was about 25 ms with the raise time of 7 ms. Magnetization was obtained by integrating the voltage induced in a compensated coil system surrounding the sample. Every measurement was corrected for a background which was taken at the same conditions without the sample. The obtained curve was scaled to DC magnetization data in order to get the absolute value of the magnetic moment. A detailed description of the setup is provided elsewhere [13].

Specific-heat measurements were carried out by a relaxation method using a Quantum Design PPMS-9T. The data were collected at zero magnetic field in the temperature range 2–300 K and under applied fields 3, 6, and 9 T in the temperature range 2–20 K.

ESR studies were carried out using an X-band ESR spectrometer CMS 8400 (ADANI) ($f \approx 9.4 GHz$, $B < 0.7 T$) equipped with a low-temperature mount, operating in the range $T = 6$–300 K. The effective g factor of our sample has been calculated with respect to an external reference for the resonance field. We used (a,g-bisdiphenylene-b-phenylallyl) with g factor $g = 2.00359$ as a reference material.

NMR measurements were performed with a Tecmag Redstone pulsed spectrometer at fixed frequencies $\nu = 12$ and 79.36 MHz. The spectra were collected by step-by-step sweeping the field and integrating the echo signal obtained by the standard Hahn echo-pulse sequence at each field step. The longitudinal nuclear spin relaxation rate T_1^{-1} was measured with saturation recovery and stimulated echo-pulse protocols. For analysis of the NMR results the static magnetization data in the field 1 and 7 T have been used [10].

NPD measurements of Na$_2$MnTeO$_6$ were carried out at the SINQ spallation neutron source at PSI using two different diffractometers: DMC (cold neutron powder diffractometer) and HRPT (high-resolution thermal powder diffractometer). For the crystal structure refinement, data from HRPT were obtained with two neutron wavelengths, $\lambda = 1.494$ Å and $\lambda = 1.886$ Å, using focusing monocrystalline germanium monochromator with Ge reflections (335) and (115), respectively. The fixed takeoff angle of the monochromator $2\theta_M$ was $120°$. NPD patterns were obtained in the range of 2θ diffraction angles from $3.55°$ to $164.50°$ with a step of $0.05°$. The sample was placed in a thin-walled cylindrical vanadium container $\phi 6$ mm $\times 50$ mm. HRPT measurements at room temperature were carried out to additionally check the quality of the sample, its stoichiometry, and refinement of its crystal structure using a high-resolution instrument. To
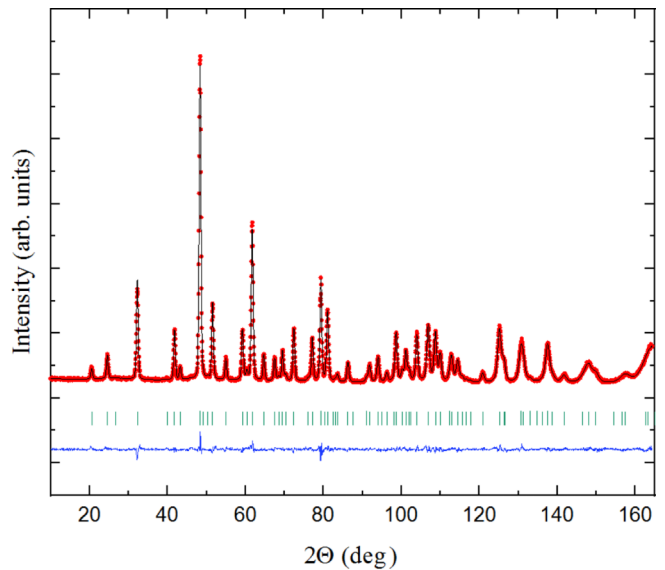

FIG. 1. Experimental HRPT neutron diffraction pattern obtained at $T = 300$ K with wavelength $\lambda = 1.49$ Å and Rietveld refinement results for Na$_2$MnTeO$_6$. The red dots represent the experimental data, the black line shows the calculated intensity, the green ticks indicate the positions of the nuclear Bragg reflections, and the blue line shows the difference between experimental and calculated data, plotted at the bottom for convenience.

study the magnetic scattering of neutrons associated with long-range magnetic order, measurements were carried out at the lowest available temperature, $T = 1.6$ K. An analysis of these experimental data made it possible to construct and describe the spin structure in the ground state. To study the dependence of magnetic scattering on temperature, experiments were performed on the high-intensity powder diffractometer DMC. The measurements were carried out at a wavelength $\lambda = 2.4575$ Å using a graphite monochromator. NPD patterns were collected in the 2θ diffraction angle range of $5.0°$–$86.7°$ with a step of $0.1°$ at temperatures $T = 1.6, 2.5, 4, 6, 10,$ and 20 K. All NPD experimental data from HRPT and DMC were processed by the Rietveld method in the FULLPROF program [14].

III. RESULTS AND DISCUSSION

A. Neutron powder diffraction: Crystal structure

The NPD pattern measured on the HRPT at room temperature and results of Rietveld refinement are shown in Fig. 1. The crystal structure of Na$_2$MnTeO$_6$ has already been studied on the laboratory x-ray diffractometer, where it was determined that it belongs to the space group $P\bar{3}1c$ [10]. In the present work, this model was confirmed and somewhat refined due to the use of neutron diffraction and the high resolution of the HRPT diffractometer. The proposed structural model perfectly describes all diffraction peaks; no impurities were found. To refine the crystal structure, we used the data obtained at $T = 300$ K with a short neutron wavelength $\lambda = 1.49$ Å.

Given the significant difference in magnitude and even sign in neutron scattering lengths for Na (3.63 fm), Mn (-3.73 fm),

TABLE I. Atomic coordinates (x, y, z), sites occupations (Occ) and isotropic thermal Debye-Waller factors (B_{iso}) and agreement factors of the Rietveld refinement for Na_2MnTeO_6. Space group $P\bar{3}1c$, $a = b = 5.11576(3)$ Å, $c = 10.5701(9)$ Å.

Atom	Site	x	y	z	Occ	B_{iso}
Na	$4f$	2/3	1/3	0.9620(2)	1/3	0.81(3)
Mn	$2d$	2/3	1/3	1/4	0.154(1)	0.49(5)
Mn	$2a$	0	0	1/4	0.008	
Te	$2a$	0	0	1/4	0.154	0.53(4)
Te	$2d$	2/3	1/3	1/4	0.013	
O	$12i$	0.0522(1)	0.7150(1)	0.6480(4)	0.988(3)	0.73(1)

$R_p = 2.88$, $R_{wp} = 3.67$, $R_{exp} = 2.34$, $R_B = 1.99$, $\chi^2 = 2.47$. Mn ions have been placed in the Te position and vice versa to assess the possible partial site inversion.

and Te (5.80 fm) [15], it was possible to determine the stoichiometry by refining the occupation of each site. Neutron diffraction measurements are also important for analyzing the possible existence of antisite defects, which are often found in such layered oxides. In our case, this is a partial inversion of the Mn/Te positions, which can cause deviations from the assumed oxidation states of Mn and Te, especially in the case of the possible oxygen nonstoichiometry. Finally, Rietveld refinement of room-temperature neutron diffraction data led to $Na_{1.95(1)}Mn_{0.98(2)}Te_{1.00(1)}O_{5.93(4)}$, within experimental error of the intended stoichiometry.

Thus, we do not observe any deviation from stoichiometry for manganese and tellurium. However, there is a mixing in the distribution of Mn and Te ions over their sites of about 7% (Table I), not previously determined by other techniques. In addition to the quite expected oxygen nonstoichiometry, we also note a slight sodium deficiency.

To improve the quality of the fits, a microstructural analysis was carried out taking into account the "size" features of the crystalline structure of the sample. The effect of "strain" turned out to be insignificant. The structural parameters–the position of all atoms in the unit cell, occupation of positions,

thermal factors, bond lengths, and bond angles, which affect the magnetic properties of the material under study, are summarized in Table I and Table S1 [16].

An increase in the ionic radii in the A position from Li^+ ($r_{Li}^{VI} = 0.90$ Å) to Na^+ ($r_{Na}^{VI} = 1.16$ Å) results in the increase in the unit-cell dimensions; very differently in layers and between them, the lattice parameter c changes by 11% whereas a varies by only 2%. So, parameter a of the sodium compound differs from parameter a of the lithium sample by ~ 0.1 Å, whereas, for parameter c, the corresponding difference is 1.0 Å. Comparison of the values of the fine fragments of the crystal lattice, namely the interatomic distances and bond angles, of the two compounds Li_2MnTeO_6 and Na_2MnTeO_6 (Table S1) shows that the method of synthesis, direct synthesis, or exchange reactions, of these samples does not affect the type of their crystal structures. The differences are determined only by the size of the ion in the A position ($4f$ site).

The Na_2MnTeO_6 compound is based on layers of oxygen octahedra with common edges, the center of which is occupied by Mn^{4+} and Te^{6+}, and these two types of octahedra are almost completely ordered, as shown in Fig. 2(a). Their conjugation with the NaO_6 octahedra forming layers above and below is completely different. The NaO_6 octahedra share two opposite faces with the MnO_6 octahedra and common vertices with the TeO_6 octahedra. As a result, passing from the $(MnTeO_6)^{2-}$ layer to the next one along the c axis, a zigzag arrangement of magnetic manganese ions could be observed.

The crystal structure of the sample under study provides the conditions necessary for the occurrence of frustrated exchange interactions in the magnetic subsystem. Despite the fact that the compounds crystallize into the $P\bar{3}1c$ space group, where the Mn^{4+} and Te^{6+} cations together form honeycomb layers [Fig. 2(b)], which alternate with nonmagnetic layers consisting of Na^+ cations, the magnetic sublattice of manganese ions is based on triangular geometry. Each separate $(MnTeO_6)^{2-}$ layer is ordered so that the magnetic Mn^{4+} ions form a triangular network, which, in the presence of the antiferromagnetic (AFM) type of spin ordering of manganese
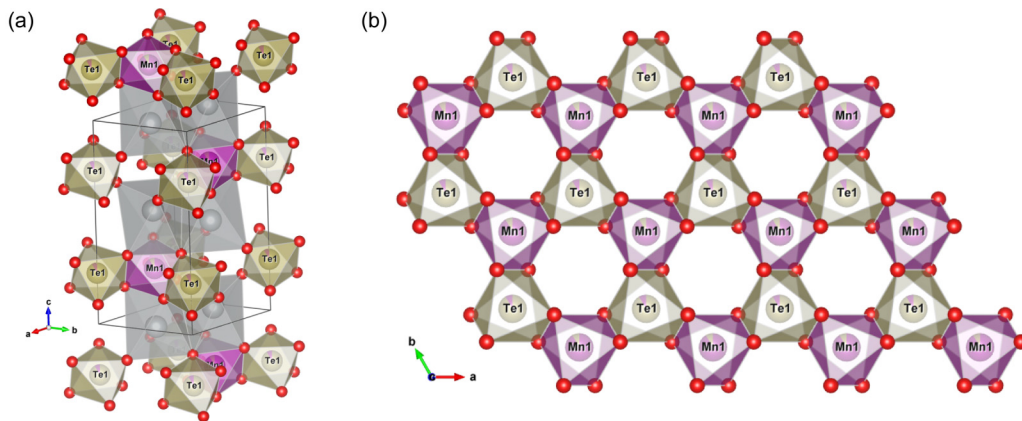

FIG. 2. (a) Polyhedral view of the layered crystal structures of Na_2MnTeO_6. The NaO_6, MnO_6, and TeO_6 octahedra are in gray, pink, and gold, respectively. Red circles represent the O atoms. Solid lines mark the crystallographic unit cell. (b) The projection of the magnetic layer $(MnTeO_6)^{2-}$ on the ab plane, in which the MnO_6 and TeO_6 octahedra alternate sharing their edges. The pink and gold octahedra represent the MnO_6 and TeO_6, respectively.
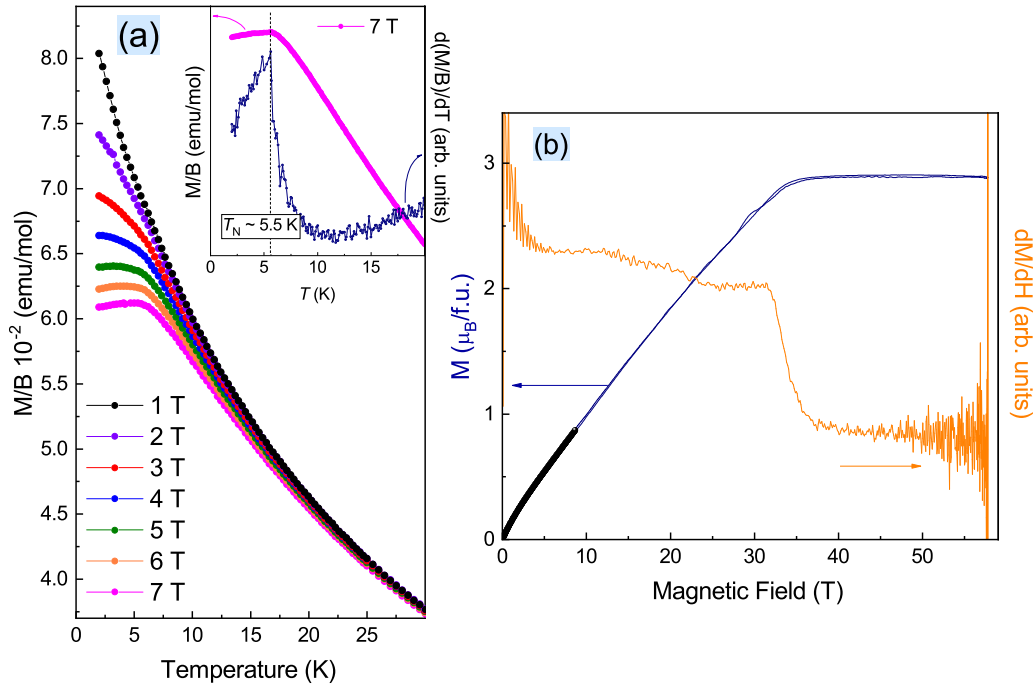
FIG. 3. (a) The temperature dependencies of $\chi(T)$ in Na_2MnTeO_6 taken at various magnetic fields in the field-cooled regime. Inset: zoom of the low-temperature region and the first derivative of the magnetization curve. (b) Magnetization M and its derivative dM/dH measured at $T = 1.4$ K. Solid lines represent the data measured in the pulsed field; solid symbols correspond to DC measurement.

ions, can lead to frustrations in the magnetic system. In a layer thus organized, weak super-super-exchange through the Mn-O-Te-O-Mn path becomes possible.

B. Magnetization

The magnetic susceptibility $\chi(T)$ of Na_2MnTeO_6 taken at lowest magnetic field 1 T exhibits the Curie-Weiss law at elevated temperatures evidencing no pronounced anomalies down to 2 K, as shown in Fig. 3(a). At increasing magnetic field, the anomaly develops signaling magnetic phase transition at $T = 5.5$ K. The peak in $d\chi/dT$ vs T dependence shown in the inset to Fig. 3(a) corresponds to the onset of an antiferromagnetic order.

The $M(H)$ dependence measured at $T = 1.4$ K for Na_2MnTeO_6 is shown in Fig. 3(b). Magnetization grows monotonously until saturation is reached at about 34 T. Saturation moment amounts to $2.9\,\mu_B$, which is in a reasonable agreement with the theoretically expected saturation magnetic moment for $M_{sat} = ngS\mu_B = 2.96\,\mu_B$ for Mn^{4+} ($S = 3/2$) ions. There is a change of slope between 15 and 20 T, which can be observed as a smeared step on the derivative curve. For the powder sample available it is too risky to ascribe this development to a particular scenario possible for the $S = 3/2$ triangular structure.

C. Specific heat

In contrast to magnetic susceptibility, the temperature dependence of specific heat $C_p(T)$ at zero magnetic field demonstrates a distinct λ-type anomaly, corresponding to the onset of long-range magnetic order. According to these specific-heat data, the Néel temperature $T_N = 5.5$ K. In order to analyze

the magnetic phase transition in Na_2MnTeO_6 the temperature dependence of specific heat was also measured for its isostructural nonmagnetic analog Na_2GeTeO_6, as shown in Fig. 4(a). Assuming that this specific heat provides an estimation for the pure lattice contribution to $C_p(T)$, one can evaluate the corresponding contribution to the specific heat and entropy of studied compounds. The value of Debye temperature Θ_D has been estimated as $\Theta_D^{nonmag} = 420 \pm 5$ K for the diamagnetic compound Na_2GeTeO_6 and $\Theta_D^{mag} = 430 \pm 5$ K for Na_2MnTeO_6. For a more accurate determination of the lattice contributions $C_{lat}(T)$ to the specific heat, the standard scaling procedure [17] was carried out, as represented by a solid line in Fig. 4(a). It was established that the jump of magnetic specific heat $\Delta C_m = 7.9$ J/molK is much less than one predicted from the mean-field theory for the antiferromagnetic spin ordering of for Mn^{4+} ($S = 3/2$) ions $\Delta C_m^{theor} = 5RS(S + 1)/[S^2 + (S + 1)^2] \approx 18.3$ J/mol K [18]. The corresponding value of magnetic entropy saturates at about 20 K, reaching approximately 10 J/(mol K). It is also lower than the estimation obtained from the mean-field theory $\Delta S_m^{theor} = R\ln(2S + 1) \approx 11.5$ J/(mol K). Such a reduction of the ΔC_m and the ΔS_m is quite expected for 2D triangular antiferromagnets and indicates the presence of short-range magnetic correlations at temperatures higher than the order-disorder transition [1,19]. Moreover, the analysis of the magnetic specific heat $C_m(T)$ below T_N in terms of spin-wave approach [19] $C_m(T) \sim T^{d/n}$ reveals $d = 2$ and $n = 1$ [see the inset in Fig. 4(a)], implying the predominance of 2D AFM magnons in Na_2MnTeO_6.

It was also established that the magnetic field strength increase leads to significant changes in the susceptibility behavior and the appearance of maxima on $\chi(T)$ curves at low temperatures [Fig. 2(a)]. The distinct position of T_N on
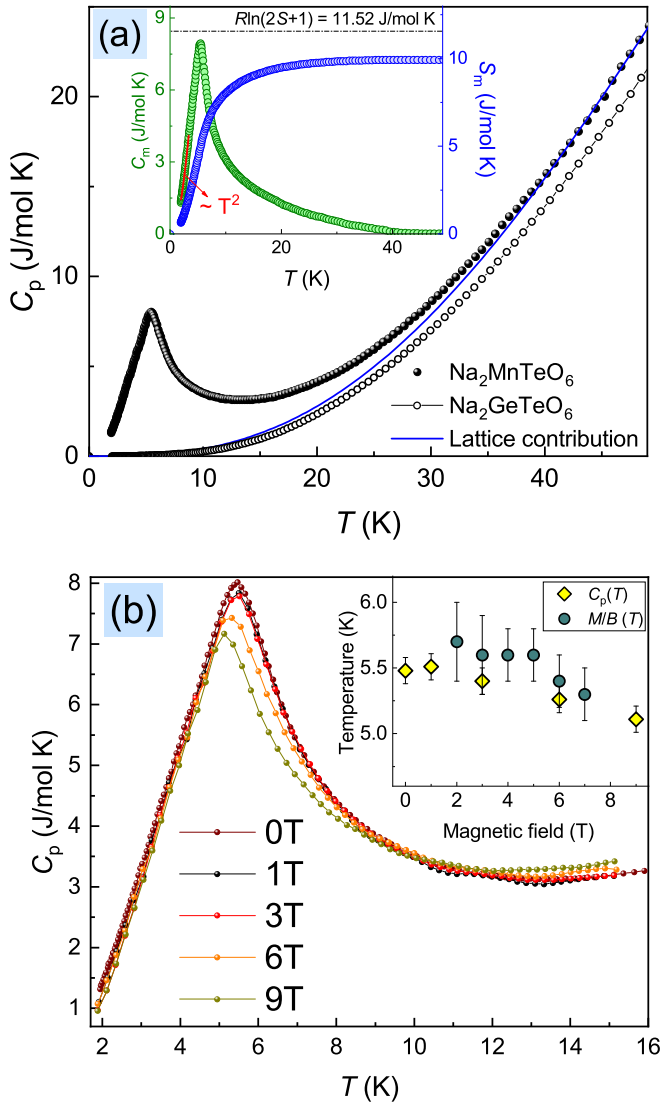
FIG. 4. (a) Temperature dependence of the specific heat $C_p(T)$ in Na_2MnTeO_6 (black filled symbols) and its nonmagnetic isostructural analogue Na_2GeTeO_6 (black open symbols) in zero magnetic field. The solid line represents the lattice contributions. Inset: the temperature dependences of $C_m(T)$ and the entropy $S_m(T)$. (b) Temperature dependences of specific heat $C_p(T)$ in Na_2MnTeO_6 at various external magnetic fields. Inset: T_N vs B dependence.

susceptibility dependence at $B = 7$ T was fixed using the first derivative (orange symbols), and it is in good agreement with the value obtained from specific-heat data. Applying the external magnetic fields also leads to a slight shift of λ-type anomaly on $C_p(T)$ to low temperatures, as shown in Fig. 4(b). The $T_N(B)$ dependence is shown in the inset to Fig. 4(b).

D. Electron spin resonance

Over the whole temperature range, the ESR spectra reveal a single resonance line, ascribed to the signal from Mn^{4+} ions, which can be described by the standard Lorentzian profile for Na_2MnTeO_6 (Fig. S1, Ref. [20]; also, see Ref. [1] therein). The values of the effective g factor and the linewidth ΔB
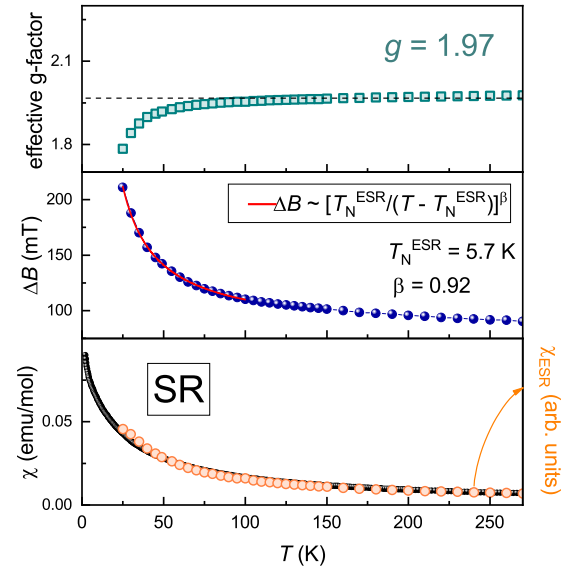

FIG. 5. Temperature dependencies of the effective g factor, the ESR linewidth ΔB, and also the integral ESR intensity (in comparison with the static susceptibility) for Na_2MnTeO_6 derived from the ESR data. The red solid line represents approximations in accordance with the power law (see text).

derived from the fitting analyses for the ESR spectra are collected in Fig. 5. Effective g factor $g = 1.97 \pm 0.1$ was found to be isotropic and remains almost constant with the decrease in temperature to ~100 K (upper panel of Fig. 5). Upon further cooling, the shift in the resonance field occurs, indicating the appearance of the short-range fluctuations on approaching long-range ordering transition. This feature is characteristic of low-dimensional systems.

Upon cooling, the linewidth ΔB continuously increases (Fig. 5, middle panel). Such broadening of exchange-narrowed ESR line is usually observed in the antiferromagnets due to the slowing down of spin fluctuations as the critical temperature is approached from above and can be described as

$$\Delta B(T) = \Delta B^* + A\big(T^{ESR}_N / \big(T - T^{ESR}_N\big)\big)^\beta. \quad (1)$$

Here, A is an empirical parameter, ΔB^* is the high-temperature limiting value of the linewidth, T^{ESR}_N is the temperature of the order-disorder transition, and β is a critical exponent. The value of $T^{ESR}_N = 5.7 \pm 0.5$ K is close to the value of the Néel temperature T_N, obtained from the specific-heat data. The critical exponent β tends to 1, significantly exceeding 1/3, which is characteristic of 3D Heisenberg antiferromagnets [21,22]. The obtained critical exponent clearly indicates the two-dimensional nature of exchange correlations in the studied compound. The integrated ESR intensity χ_{ESR}, obtained by the double integration of the first derivative absorption line, is shown in the lower panel of Fig. 5 along with static magnetic susceptibility. Obviously, static and dynamic susceptibilities agree quite well with each other.
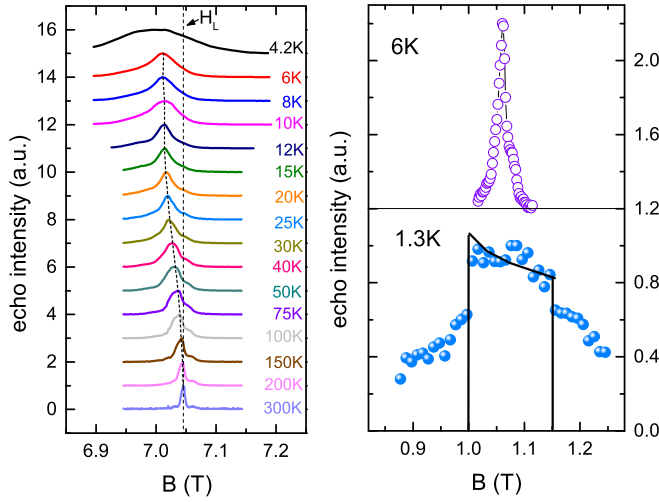
FIG. 6. The temperature evolution of ^{23}Na NMR spectra taken at 79.36 MHz (left panel).^{23}Na NMR spectra taken at 12 MHz at low temperatures; solid line is the fitting by Eq. (2) (right panel).

E. Nuclear magnetic resonance

NMR measurements on the powder sample of Na$_2$MnTeO$_6$ were performed on the ^{23}Na nuclei which possess a spin $I = 3/2$, the quadruple moment $Q = 0.104$ barn, and the gyromagnetic ratio $\gamma_n = 11.2685$ MHz/T. Since the effect of an external field on local magnetic characteristics is of particular interest, the measurements were carried out at two frequencies, 12 and 79.36 MHz, in an external field of about 1 and 7 T, correspondingly. The evolution of spectra taken at 7 T in the range 6–300 K is shown in the left panel of Fig. 6. The powder shape of the spectrum is typical for the $I = 3/2$ nucleus in the presence of a slightly anisotropic hyperfine field and a quadrupole splitting of about 200–500 kHz. The spectrum broadens with cooling and changes its shape at the lowest temperatures. The right panel of Fig. 6 shows spectra at 12 MHz taken both above (upper panel) and below (lower panel) the Néel temperature. At $T < T_N$, the spectral profile is no longer Gaussian but rectangular with broad quadrupole background which is typical for the powder line shape in antiferromagnetically ordered compounds. Such rectangular profile is described by the formula

$$f(H, H_0, H_A) \sim (4H_A)^{-1}\big(1 + \big(H_0^2 - H_A^2\big)/H^2\big), \quad (2)$$

where $H_0 = \omega_L\gamma_n$ is a Larmor field and H_A is the internal field magnitude at the position of the sodium nucleus [23]. Calculation within the framework of the dipole field model shows that magnetically nonequivalent sodium positions differ only in the direction of the local field but not its magnitude. Experimentally found value $H_A = 0.078$ T is somewhat lower than the calculated dipole field 0.148 T.

The shift of the NMR line can be defined as $k = [(B_L - B)/B_L] \times 100\%$, where B is the field of the spectral magnitude maximum and $B_L = \omega_L/\gamma_n$. Its temperature-dependent part corresponds to the local static susceptibility $k = A\chi_{loc}$, where A is the hyperfine tensor. The hyperfine interaction constant A_{hf} taken from the linear part of the $k(\chi_{bulk})$ dependences is almost the same for both external fields and determined to be

0.618 ± 0.007 kOe/μ_B. The point-moment dipole-dipole interaction model gives $A_\perp \approx 0.35$ kOe/μ_B, $A_{//} \approx 0.7$ kOe/μ_B that is close to the experimental values. The deviation of the local susceptibility k from the bulk one indicates the development of correlations in the system of manganese spins.

The nuclear relaxation process reflects the dynamics of the electron spin system. The ^{23}Na nuclear longitudinal spin-lattice relaxation rate T_1^{-1} was measured at the maximum of the spectral magnitude at 1 and 7 T. Since there is a partial overlap of the main line and quadrupole satellites in the powder spectrum with inhomogeneous broadening, the evolution of magnetization is not described by the standard formula for spin 3/2 [24], but contains a stretch coefficient b:

$$M \sim M_0(0.1 \exp(-\tau/T_1)^b + 0.9 \exp(-6\tau/T_1)^b). \quad (3)$$

This coefficient is about 0.8 at high temperatures and decreases to 0.6 with a sharp line broadening at low temperatures. The relaxation rate at both external fields exhibits a peak at $T \sim 5.5$ K indicating the magnetic phase transition. Basically, in magnetic materials the nuclear spin-lattice relaxation rate T_1^{-1} is a function of local dynamic spin susceptibility [25]:

$$T_1^{-1} = \frac{k_B T}{\hbar^2} \sum_q |A(\boldsymbol{q})|^2 \frac{\chi''(q, \omega_L)}{\omega_L}, \quad (4)$$

where $A(\boldsymbol{q})$ is a form factor depending on the q vector, k_B is the Boltzmann constant, ω_L is the Larmor frequency, and χ'' is the imaginary part of the dynamic susceptibility. Therefore, in the paramagnetic regime $(T_1T)^{-1}$ is proportional to the static bulk susceptibility. Loss of proportionality means the appearance of a difference between the bulk static susceptibility and local dynamic one, which indicates the development of correlations and the slowing down of magnetic fluctuations. Indeed, the deviation of the local dynamic susceptibility from the bulk static one obtained in the same magnetic field occurs at the same temperatures as for the line shift k, as shown in the left panel of Fig. 7. Relaxation in this temperature range can be described in terms of the critical exponent

$$T_1^{-1}/T_{1\infty}^{-1} \sim ((T - T_N)/T_N)^{-p}, \quad (5)$$

where $p = \nu(z-\eta)$ [26]. At temperatures of 6–15 K and 8–35 K for fields 7 and 1 T, the value of the parameter $p = 0.268 \pm 0.023$ and 0.168 ± 0.0106, respectively, as shown in the right panel of Fig. 7. Obtained values of the critical parameter are extremely small and cannot be attributed to 3D correlations where $0.5 \leqslant p \leqslant 1.2$ and even to 2D Ising case in the square lattice where $p \approx 1.9$ [3]. Apparently, this indicates that for the critical regime in Na$_2$MnTeO$_6$ the geometry of magnetic planes is significant. Monte Carlo simulations give a relatively small value of correlation length exponent $\nu \approx 0.5$ [27] and $z = 0.64$ [28] for triangle lattice, which sets the upper limit for p as 0.32. Taking into account that η, as calculated [28], can reach a value of 0.5 in triangular systems, one can expect extremely low values of p. Therefore, NMR results indicate that in a wide temperature range below 35 K, the correlations which are specific for a two-dimensional triangular lattice develop in the Na$_2$MnTeO$_6$ magnetic system.

An extended temperature range of spin correlations was also observed in other systems with a triangular lattice using
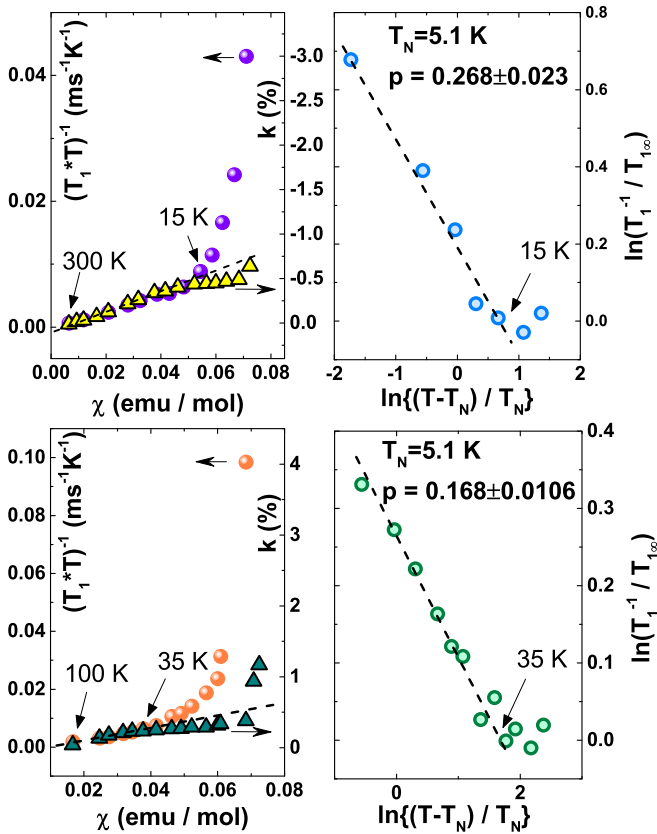
FIG. 7. Dependences of the local static k (open triangles) and dynamic $(T_1 T)^{-1}$ (solid circles) susceptibility on static bulk susceptibility at 7 T (top) and 1 T (bottom) (left panel). ln-ln plots of ^{23}Na nuclear spin-lattice relaxation rates normalized to the high-temperature value vs the reduced temperature $(T - T_N)/T_N$ at 7 T (top panel) and 1 T (bottom panel). Dashed lines correspond to Eq. (5) (right panel).

the NMR technique [29]. Such correlations in Na_2MnTeO_6 have been observed to be very sensitive to the influence of an external magnetic field, which easily disturbs an equilibrium in a triangular frustrated magnetic lattice. For Na_2MnTeO_6 the temperature of the development of correlations decreases more than in two times in field 7 T comparing to 1 T. In close vicinity of the Néel temperature, the critical parameter p rises sharply, denoting a 3D nature of the AFM transition, but due to the insufficient number of experimental points, it cannot be determined accurately.

F. Neutron powder diffraction: Magnetic structure

The temperature evolution of neutron scattering from the Na_2MnTeO_6 sample is shown in Fig. 8(a). The appearance of additional reflections below 6 K and their existence at lower temperatures in comparison with neutron diffraction patterns measured at higher temperatures is clearly seen. The neutron magnetic scattering is associated with the long-range order of Mn^{4+} ions moments. The appearance of magnetic scattering at diffraction angles smaller than the position $2\theta \approx 27°$ of the first nuclear reflection (002) indicates the AFM nature of the formed magnetic order. The phase transition from the paramagnetic state to the AFM with decreasing temperature is observed without any noticeable structural transformations. Figure 8(b) clearly shows the distinction between the first magnetic Bragg reflections in Na_2MnTeO_6 and Li_2MnTeO_6. The difference in Bragg peak positions indicates different propagation vectors of the magnetic structure.

Analysis of the positions of the most intense magnetic reflections shows that the propagation vector is $\mathbf{k} = (1/3, 1/3, 1/3)$. After sorting out possible magnetic configuration for this propagation vector with the help of the BASIREP program from the FULLPROF suite we have found the solution for the magnetic structure in the maximum symmetry magnetic Shubnikov space group $R\bar{3}'c'$ (No. 167.4.1337) [30,31]. The basis transformation from the parent paramagnetic crystal unit cell and the magnetic one is given by the relationship $A = 2a + b, B = -a + b, C = 3c$, where the capital letter and lower case are the basis vectors of the magnetic and the parent paramagnetic space group, respectively.
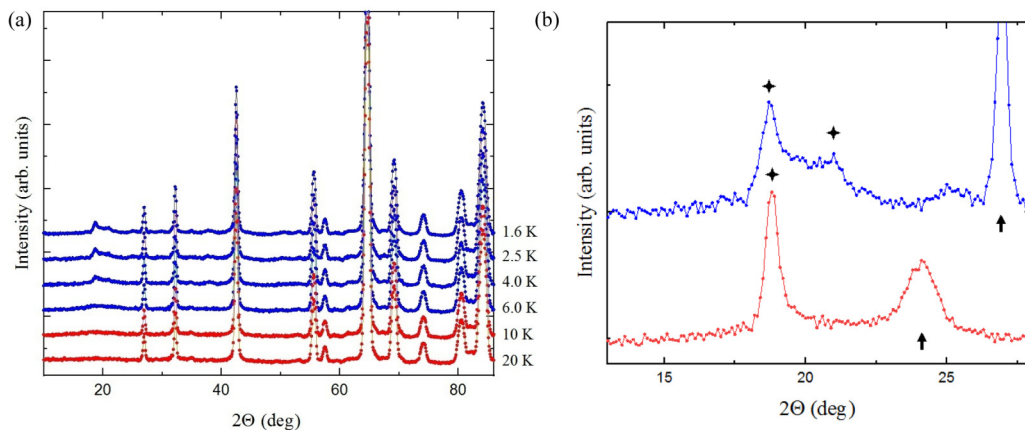

FIG. 8. (a) Neutron diffraction patterns of Na_2MnTeO_6 measured on DMC diffractometer at low temperatures. The patterns from the sample in the paramagnetic state are marked in red; the patterns from the sample with emerging long-range AFM ordering are in blue. (b) Small-angle part of the low-temperature neutron diffraction patterns for Na_2MnTeO_6, and Li_2MnTeO_6 measured on the HRPT diffractometer. The stars indicate the first additional reflections with diffraction angles less than the position of the first nuclear reflection (002) (which is marked with an arrow for each compound) associated with the formation of long-range magnetic order of the AFM type.
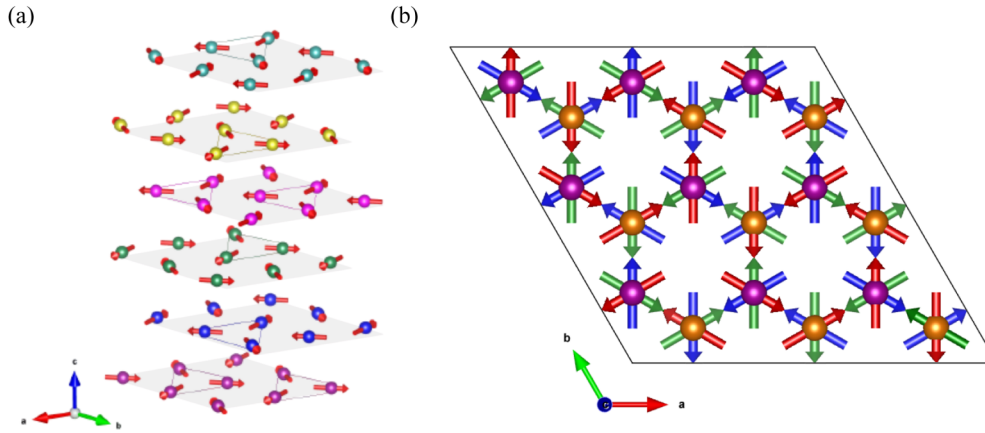
FIG. 9. (a) Spin structure of Na_2MnTeO_6 compound. Ions belonging to various layers are shown in different colors. Spin triangles are marked by solid lines. (b) Projection of the magnetic structure onto the *ab* plane. The three ordering layers are marked with different arrow colors. Ions at neighboring levels along the *z* coordinate and varying in the direction of spin are shown in different colors as well.

The magnetic structure of Na_2MnTeO_6 in the ground state obtained by the Rietveld refinement of the experimental neutron diffraction data and their symmetry analysis is shown in Fig. 9. Magnetic ions in an octahedral oxygen environment form a triangular network. There are six layers of antiferromagnetically ordered manganese ions per unit magnetic cell, ordered like a spin helicoid along the crystallographic direction *c*, as shown in Fig. 9(a).

In the projection onto the *ab* plane shown in Fig. 9(b), the manganese ions are arranged so that their spins lie in the plane, forming a 120° structure. Triangular spin ordering is realized inside each layer. In this case, when passing from layer to layer, the spins of manganese atoms in the position (2/3 1/3 1/4) rotate 120° clockwise, and the spins of atoms in the position (1/3 2/3 1/4) counterclockwise. The spins in each spin triangle are directed away from the center of the triangle in the layer, in contrast to Li_2MnTeO_6, in which the direction of the spins changes from "inward" to "outward" when passing from layer to layer.

IV. CONCLUSIONS

We studied magnetic ordering as well as static and dynamic properties of Na_2MnTeO_6 belonging to the layered quaternary tellurate family with honeycomb crystal and triangular magnetic lattice using a combination of high-resolution neutron powder diffraction, magnetization, specific heat, electron spin resonance, and nuclear magnetic resonance measurements.

Magnetic properties of the compounds within this family appear to be quite sensitive to interlayer exchange interactions associated with the distances between the layers. The strong nearest-neighbor interlayer coupling expected for Li_2MnTeO_6 leads to planar spin order in the ground state described by the propagation vector (1/3, 1/3, 0). This rigid magnetic structure is formed by a staggered arrangement of 120° triangles with opposite directions of spins in adjacent layers.

The competition of nearest-neighbor and next-nearest neighbor interlayer exchange interactions in Na_2MnTeO_6 leads to the formation of a helicoidal spin ordering, described by the propagation vector (1/3, 1/3, 1/3) also with a 120° triangular order in one layer, but with the same directions

of spins directed away from the center of the triangle in adjacent layers. The order along the *c* axis, i.e., perpendicular to the layers, is fully dictated by the ratio of competing nearest-neighbor J_{nn} and next-nearest neighbor J_{nnn} exchange interactions parameters. It has been shown in first-principles calculations for Li_2MnTeO_6 that the interlayer exchange is very small and even change sign from ferromagnetic to antiferromagnetic at variation of Hubbard energy.

Elementary calculations of exchange energy,

$$E = J_{nn}S^2\cos\varphi + J_{nnn}S^2\cos2\varphi, \quad (6)$$

show that 120° helical spin structure of manganese *S*, corresponding to (1/3, 1/3, 1/3) propagation vector, forms at $J_{nn} < 2J_{nnn}$. Evidently, the increase of interlayer distance by 11% in Na compound in comparison with Li compound results in weakening of nearest-neighbor J_{nn} exchange interaction parameter as compared to next-nearest neighbor J_{nnn} exchange interaction parameter.

Magnetic resonance (ESR and NMR) data demonstrate the emergence of an extended temperature region of increasing magnetic correlations highly above the Néel temperature. These correlations are strongly two dimensional and become three dimensional only in the closest vicinity of the magnetic phase transition. The specific-heat measurements also indicate the presence of short-range magnetic correlations at temperatures higher than the order-disorder transition.

Thus, a comparative study of Na_2MnTeO_6 and Li_2MnTeO_6 has revealed an important aspect of the effect of interlayer coupling on magnetism in layered quasi-two-dimensional magnets with frustrated interaction within the layers, in the case when magnetic ions form a triangular antiferromagnetic structure. Evidently, the slight variations in interlayer exchange interactions leads to a qualitative change in the ground magnetic state resulting in different spin orders.

---

[1] A. Vasiliev, O. Volkova, E. Zvereva, and M. Markina, Milestones of low-D quantum magnetism, npj Quantum Mater. **3**, 18 (2018).

[2] M. F. Collins and O. A. Petrenko, Triangular antiferromagnets, Can. J. Phys. **75**, 605 (1997).

[3] L. Savary and L. Balents, Quantum spin liquids: A review, Rep. Progr. Phys. **80**, 016502 (2017).

[4] O. V. Yakubovich, L. V. Shvanskaya, G. V. Kiriukhina, A. S. Volkov, O. V. Dimitrova, and A. N. Vasiliev, Hydrothermal synthesis and a composite crystal structure of $Na_6Cu_7BiO_4(PO_4)_4[Cl, (OH)]_3$ as a candidate for quantum spin liquid, Inorg. Chem. **60**, 11450 (2021).

[5] O. V. Maximova, S. V. Streltsov, and A. N. Vasiliev, Long range ordered, dimerized, large-D and Haldane phases in spin 1 chain compounds, Crit. Rev. Solid State Mater. Sci. **46**, 371 (2021).

[6] A. Neubauer, C. Pfleiderer, B. Binz, A. Rosch, R. Ritz, P. G. Niklowitz, and P. Boni, Topological Hall Effect in the A Phase of MnSi, Phys. Rev. Lett. **102**, 186602 (2009).

[7] S. Seki, Y. Onose, and Y. Tokura, Spin-driven Ferroelectricity in Triangular Lattice Antiferromagnets ACrO2 (A = Cu, Ag, Li or Na), Phys. Rev. Lett. **101**, 067204 (2007).

[8] H. B. Cao, A. Banerjee, J. Q. Yan, C. A. Bridges, M. D. Lumsden, D. G. Mandrus, D. A. Tennant, B. C. Chakoumakos, and S. E. Nagler, Low temperature crystal and magnetic structure of alpha-RuCl3, Phys. Rev. B **93**, 134423 (2016).

[9] P. M. Woodward, A. W. Sleight, L.-Sh. Du, and C. P. Grey, Structural studies and order-disorder phenomenon in a series of new quaternary tellurates of the type $A^{2+}M^{4+}Te^{6+}O_6$ and $A^{1+}_2M^{4+}Te^{6+}O_6$, J. Sol. St. Chem. **147**, 99 (1999).

[10] V. B. Nalbandyan, I. L. Shukaev, G. V. Raganyan, A. Svyazhin, A. N. Vasiliev, and E. A. Zvereva, Preparation, crystal chemistry, and hidden magnetic order in the family of trigonal layered tellurates $A_2Mn^{4+}TeO_6$ (A = Li, Na, Ag, or Tl), Inorg. Chem. **58**, 5524 (2019).

[11] E. A. Zvereva, G. V. Raganyan, T. M. Vasilchikova, V. B. Nalbandyan, D. A. Gafurov, E. L. Vavilova, K. V. Zakharov, H.-J. Koo, V. Yu. Pomjakushin, A. E. Susloparova, A. I. Kurbakov, A. N. Vasiliev, and M.-H. Whangbo, Hidden magnetic order in the triangular-lattice magnet Li_2MnTeO_6, Phys. Rev. B **102**, 094433 (2020).

[12] www.hzdr.de/hld.

[13] Y. Skourski, M. D. Kuz'min, K. P. Skokov, A. V. Andreev, and J. Wosnitza, High-field magnetization of Ho2Fe17, Phys. Rev. B **83**, 214420 (2011).

[14] www.ill.eu/sites/fullprof.

[15] V. F. Sears, Neutron scattering lengths and cross sections, Neutron News **3**, 26 (1992).

[16] See Supplemental Material at http://link.aps.org/supplemental/10.1103/PhysRevB.105.064416 for selected interatomic distances and angles for and from NPD data collected at $T = 300\,K$.

[17] D. B. Losee, J. N. McElearney, G. E. Shankle, R. L. Carlin, P. J. Cresswell, and Ward T. Robinson, An anisotropic low-dimensional Ising system, $[(CH_3)_3NH]CoCl_3 2H_2O$: Its structure and canted antiferromagnetic behavior, Phys. Rev. B **8**, 2185 (1973).

[18] A. Tari, *The Specific Heat of Matter at Low Temperature* (Imperial College Press, London, 2003).

[19] L. J. de Jongh and A. R. Miedema, Experiments on simple magnetic model systems, Adv. Phys. **23**, 1 (1974).

[20] See Supplemental Material at http://link.aps.org/supplemental/10.1103/PhysRevB.105.064416 for evolution of the ESR spectra for Na_2MnTeO_6 with decreasing temperature.

[21] K. Kawasaki, Anomalous spin relaxation near the magnetic transition, Prog. Theor. Phys. **39**, 285 (1968).

[22] K. Kawasaki, Ultrasonic attenuation and ESR linewidth near magnetic critical points, Phys. Lett. A **26**, 543 (1968).

[23] Y. Yamada and A. Sakata, An analysis method of antiferromagnetic powder patterns in spin-echo NMR under external fields, J. Phys. Soc. Jpn. **55**, 1751 (1986).

[24] A. Narath, Nuclear spin-lattice relaxation in hexagonal transition metals: Titanium, Phys. Rev. **162**, 320 (1967).

[25] T. Moriya, The effect of electron-electron interaction on the nuclear spin relaxation in metals, J. Phys. Soc. Jpn. **18**, 516 (1963).

[26] F. Borsa, M. Corti, T. Goto, A. Rigamonti, D. C. Johnston, and F. C. Chou, ^{35}Cl NMR study of spin dynamics in Sr_2CuO_2Cl, Phys. Rev. B **45**, 5756 (1992).

[27] M. L. Plumer and A. Mailhot, Tricritical behavior of the frustrated XY antiferromagnet, Phys. Rev. B **50**, 16113 (1994).

[28] G. M. Zhang and G. Z. Yang, Cluster Monte Carlo dynamics for the antiferromagnetic Ising model on a triangular lattice, Phys. Rev. B **50**, 12546 (1994).

[29] Y. Ajito, H. Kikuchi, S. Sugiyama, T. Nakashima, S. Shamoto, N. Nakayama, M. Kiyama, N. Yamamoto, and Y. Oka, Z_2 vortex-induced broadening of the EPR linewidth in the two-dimensional triangular lattice antiferromagnets, $HCrO_2$ and $LiCrO_2$, J. Phys. Soc. Jpn. **57**, 2268 (1988).

[30] N. V. Belov, N. N. Neronova, and T. S. Smirnova, Shubnikov groups, Kristallografiya **2**, 315 (1957).

[31] B. J. Campbell, H. T. Stokes, D. E. Tanner, and D. M. Hatch, ISODISPLACE: A web-based tool for exploring structural distortions, J. Appl. Crystallogr. **39**, 607 (2006).